Supporting Information

Highly efficient binary copper-iron catalyst for photoelectrochemical carbon dioxide reduction toward methane

Baowen Zhou[a,b,1], Pengfei Ou[c,1], Nick Pant[a], Shaobo Cheng[d], Srinivas Vanka[a,b], Sheng Chu[b], Roksana Tonny Rashid[b], Gianluigi Botton[d], Jun Song[c,2], and Zetian Mi[a,b,2]

a. Department of Electrical Engineering and Computer Science, University of Michigan, Ann Arbor, MI 48109, USA

b. Department of Electrical and Computer Engineering, McGill University, Montreal, QC H3A0E9, Canada

c. Department of Mining and Materials Engineering, McGill University, Montreal, QC H3A0C5, Canada

d. Department of Materials Science and Engineering, Canadian Centre for Electron Microscopy, McMaster University, Hamilton, ON L8S4M1, Canada

1. B.Z. and P.O. contributed equally to this work.

2. To whom correspondence may be addressed. Email: jun.song2@mcgill.ca or ztmi@umich.edu.

Contents

Table S1. The bond length and bond angle of CO_2 adsorbed on Cu(111) and $Fe_3O_6H_6$/Cu(111) compared to its isolated gas-phase (please also refer to Supplementary Figure 1).

Species (*CO_2)	C−O1(Å)	C−O2(Å)	O−C−O(º)
Gas phase	1.18	1.18	180.00
$Fe_3O_6H_6$/Cu(111)	1.25	1.28	126.05
Cu(111)	1.18	1.18	179.67

Table S2. Contributions to the adsorbate free energy from the zero-point energy correction, enthalpic temperature correction, entropy, and the total free energy correction, respectively. The assumed fugacity for each non-adsorbed species are also included.

Species	Fugacity (Pa)	ZPE (eV)	$\int C_p dT$ (eV)	$-TS$ (eV)
*COOH	-	0.62	0.10	-0.18
*CO	-	0.19	0.08	-0.16
*CHO	-	0.44	0.09	-0.19
*CH_2O	-	0.76	0.09	-0.19
*CH_3O	-	1.11	0.10	-0.18
*O	-	0.07	0.03	-0.04
*OH	-	0.36	0.05	-0.08
*H	-	0.16	0.01	-0.01
H_2 (ref)	101325	0.27	0.09	-0.43
CH_4	20467	1.20	0.10	-0.61
H_2O	3534	0.58	0.10	-0.66
CO_2	101325	0.31	0.10	-0.66

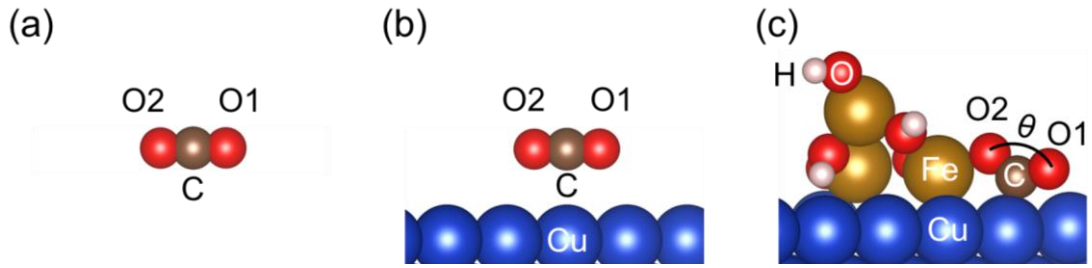

Fig. S1. The gas-phase CO_2 (a) and its optimized configuration of adsorption on Cu(111) and $FeO_3O_6H_6$/Cu(111).

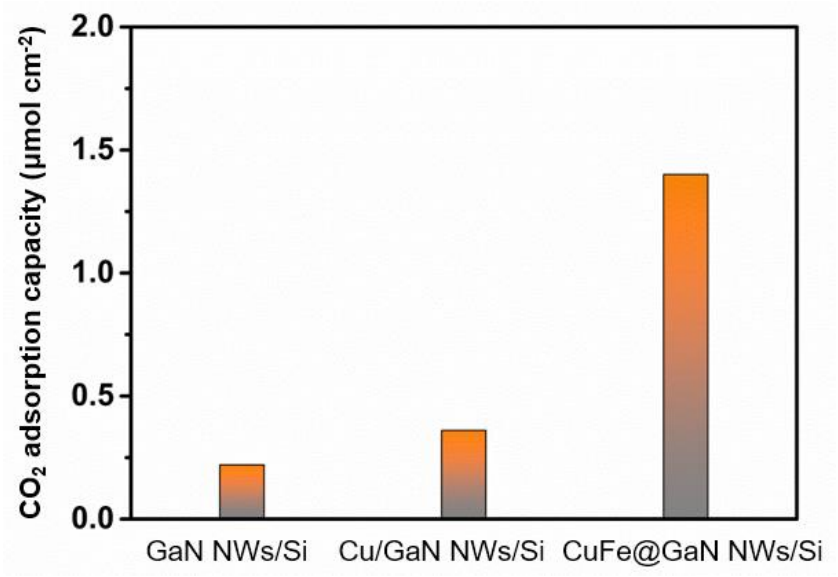

Fig. S2. CO_2 adsorption capacity of GaN NWs/Si, Cu/GaN NWs/Si, and CuFe@GaN NWs/Si.

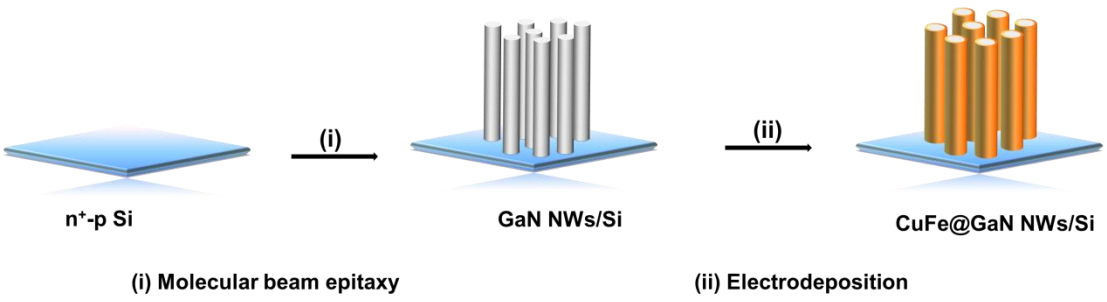

Fig. S3. Schematic illustration of synthesizing CuFe@GaN NWs/Si through molecular beam epitaxy of GaN nanowires and co-electrodeposition of Cu and Fe.

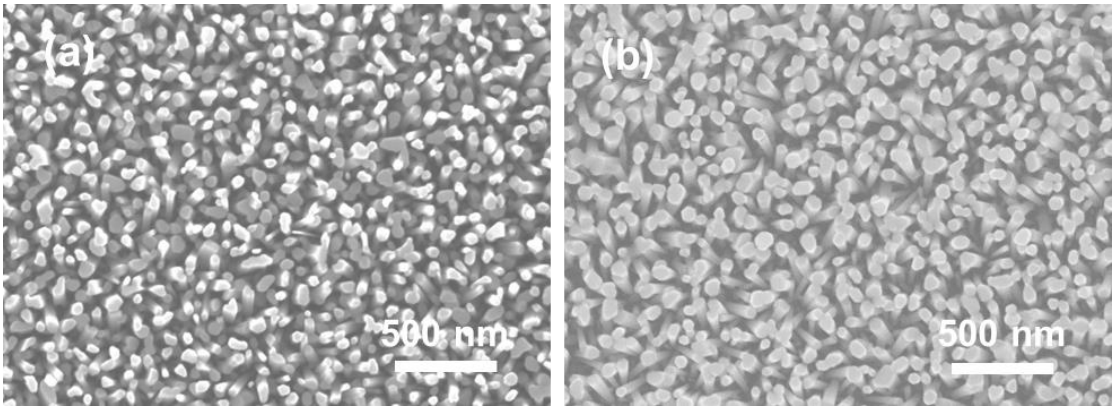

Fig. S4. Top-view SEM images of GaN NWs/Si and CuFe@GaN NWs/Si.

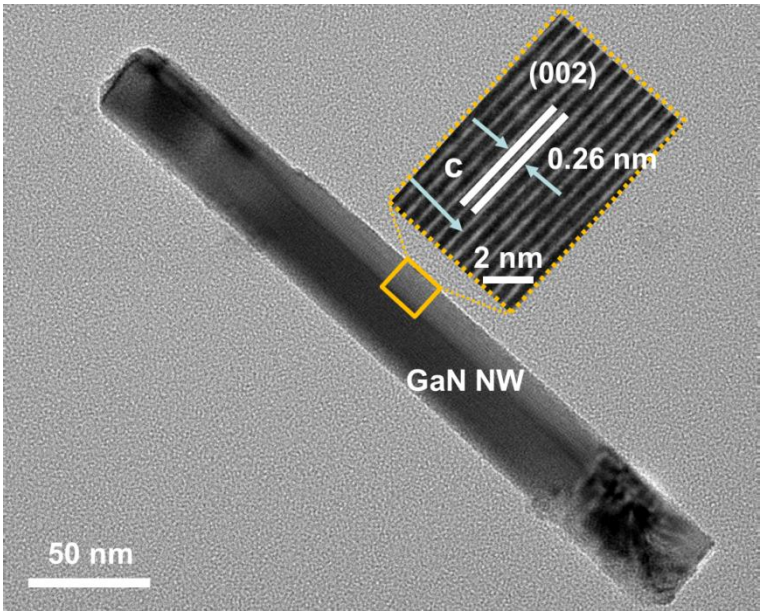

Fig. S5. TEM image of bare GaN nanowire. The inset is the high magnification image of GaN nanowire in the yellow box.

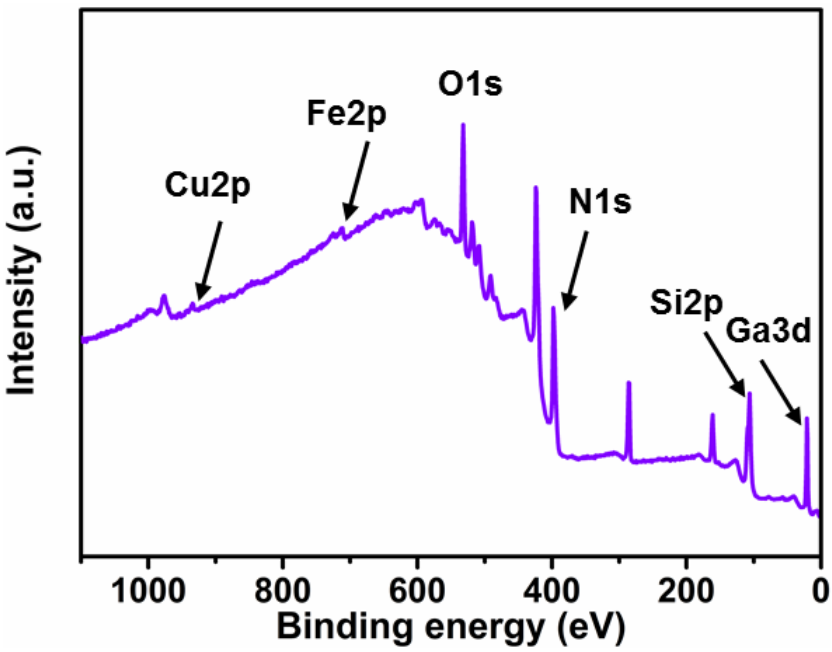

Fig. S6. X-ray photoelectron spectrum survey of CuFe@GaN NWs/Si.

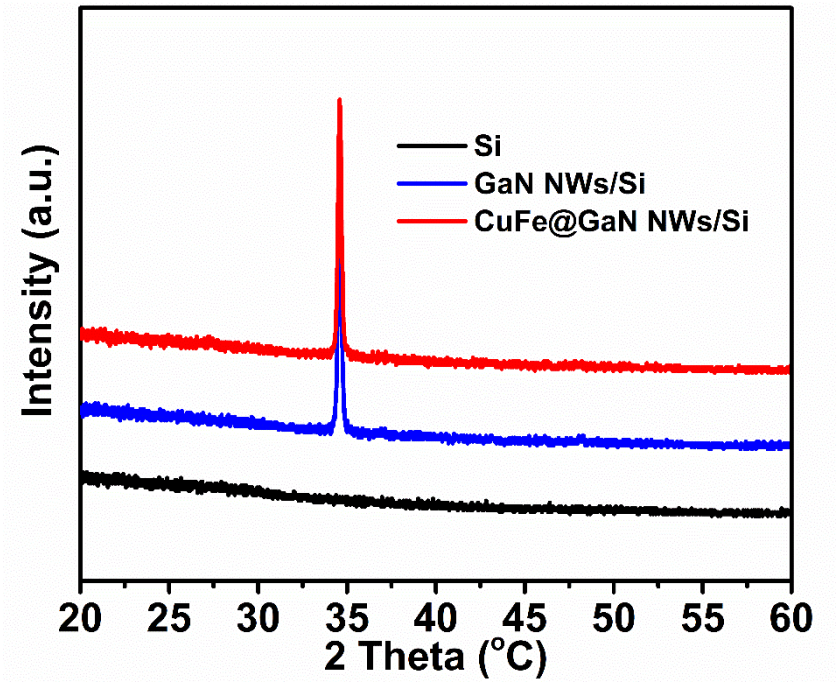

Fig. S7. X-ray diffraction spectra of n^{+}-p silicon, GaN NWs/Si, and CuFe@GaN NWs/Si.

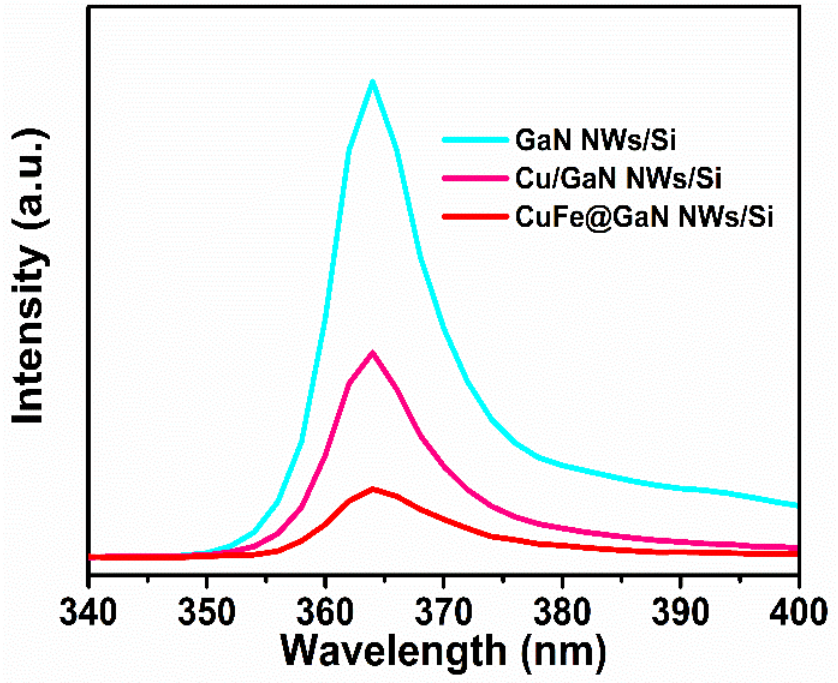

Fig. S8. Photoluminescence spectroscopy of GaN NWs/Si, Cu/GaN NWs/Si, and CuFe@GaN NWs/Si.

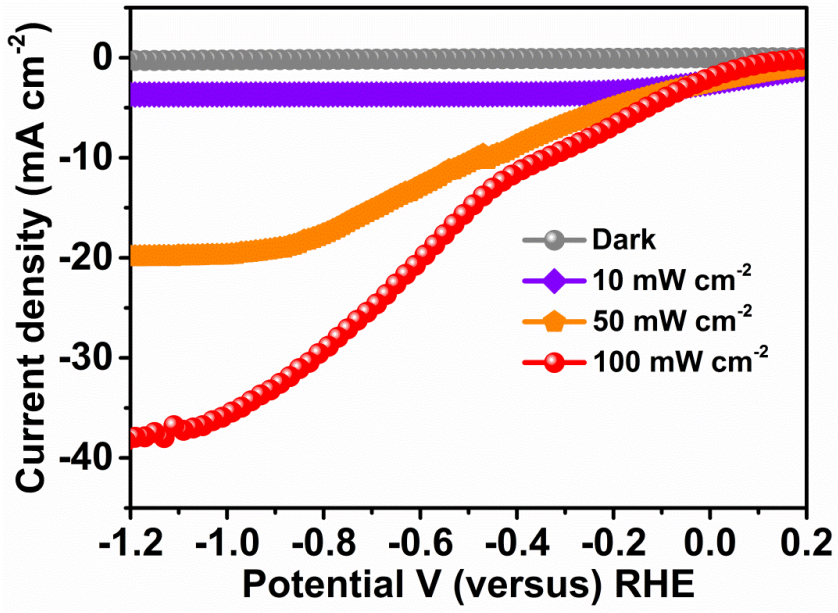

Fig. S9. Influence of the incident light intensity on the *J-V* curves of CuFe@GaN NWs/Si in CO_2-purged 0.5 M $KHCO_3$ aqueous solution.

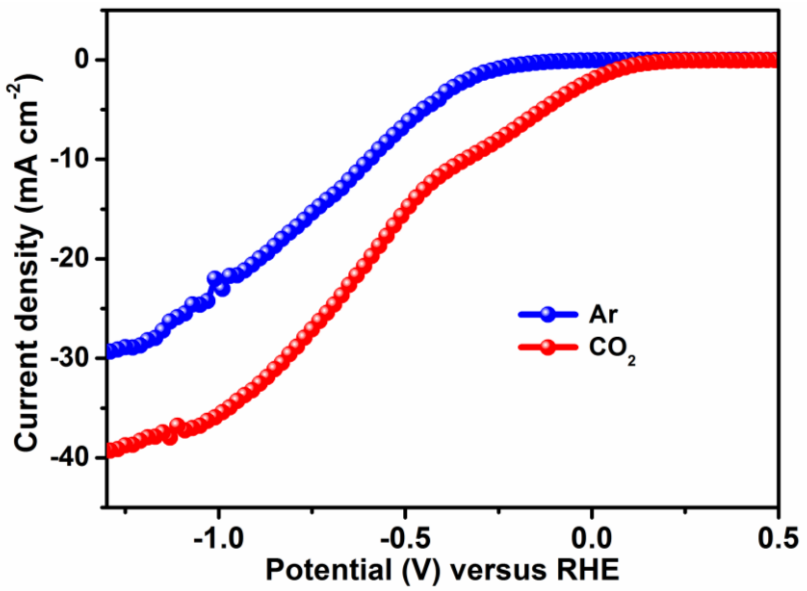

Fig. S10. *J-V* curves of CuFe@GaN NWs/Si in argon-(blue) and CO_2-(red) purged 0.5M $KHCO_3$ aqueous solution under one-sun illumination.

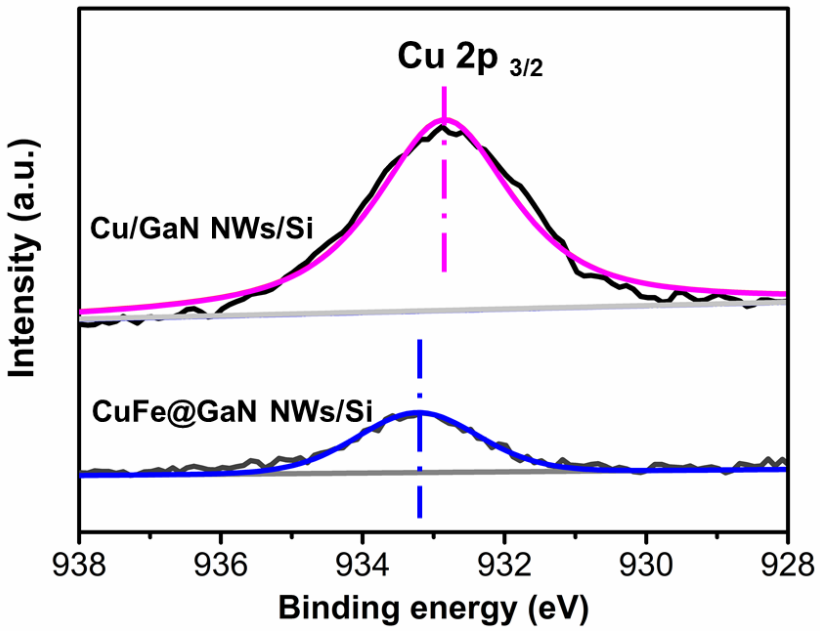

Fig. S11. XPS of Cu 2p of Cu/GaN NWs/Si (Cu 2p $_{3/2}$ = 932.9 eV) and CuFe@GaN NWs/Si (Cu 2p $_{3/2}$ = 933.2 eV).

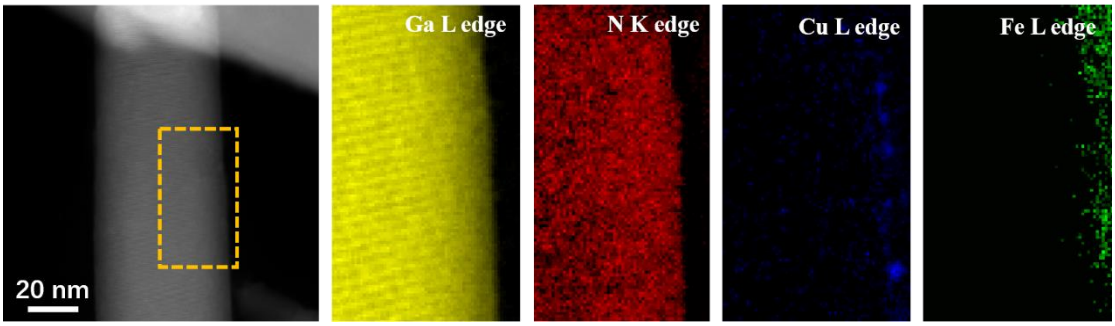

Fig. S12. STEM-HAADF image and the corresponding elemental distribution mappings of CuFe@GaN NWs/Si with Fe/Cu ratio of 4.5/1. The loading density of CuFe catalyst is ~0.033 μmol cm^{-2} measured by ICP-AES.

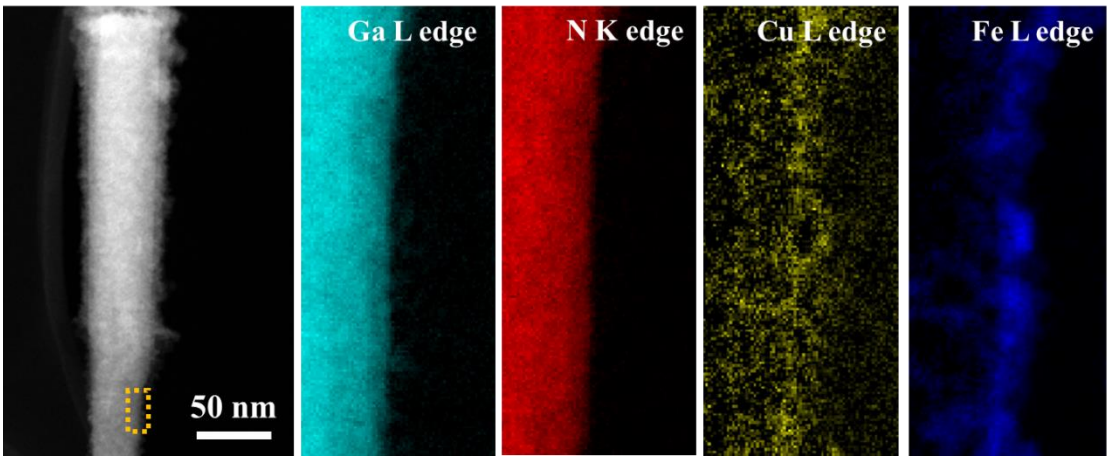

Fig. S13. STEM-HAADF image and the corresponding elemental distribution mappings of CuFe@GaN NWs/Si with Fe/Cu ratio of 12.9/1. The loading density of CuFe catalyst is ~0.075 μmol cm^{-2} measured by ICP-AES.

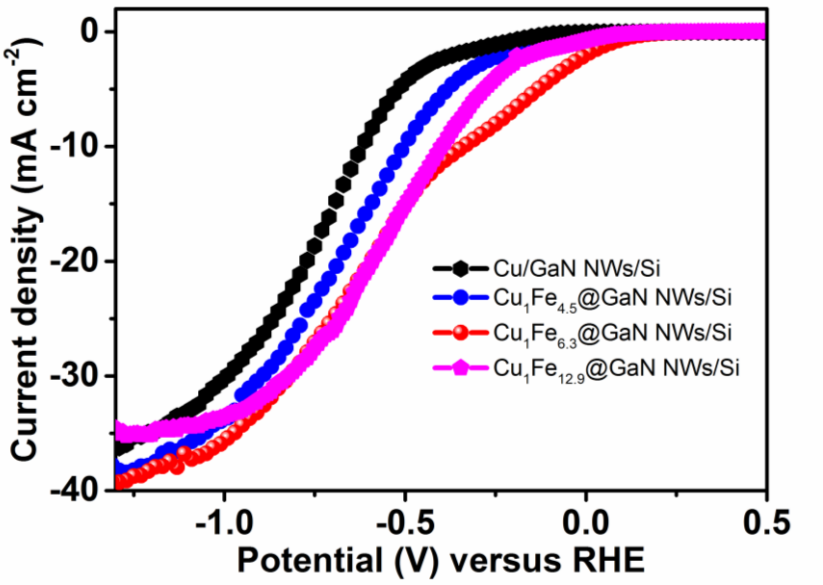

Fig. S14. *J-V* curves of Cu_xFe_y@GaN NWs/Si with different ratios of Cu to Fe in CO_2-purged 0.5 M $KHCO_3$ aqueous solution under standard one-sun illumination.

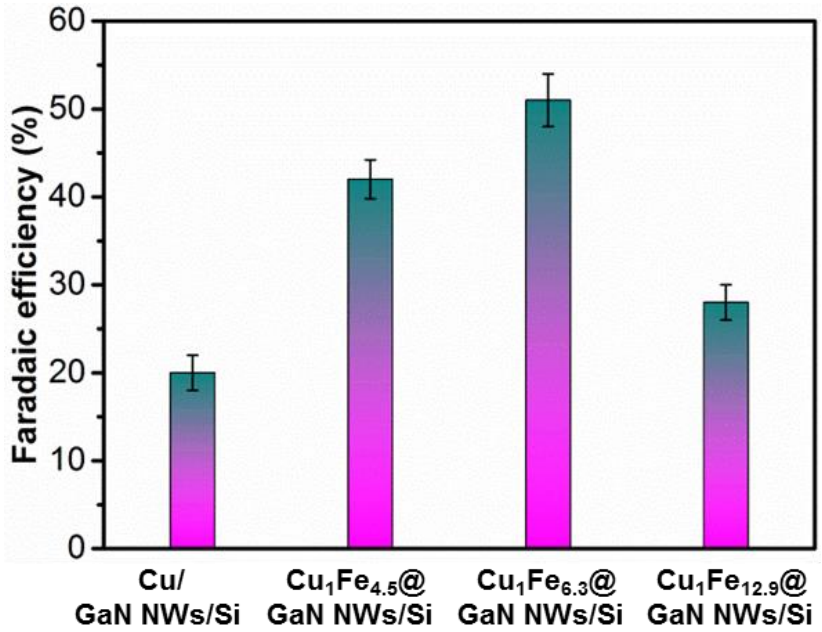

Fig. S15. Faradaic efficiencies of Cu_xFe_y@GaN NWs/Si with different ratios of Cu to Fe at -1.2 V under simulated solar irradiation.

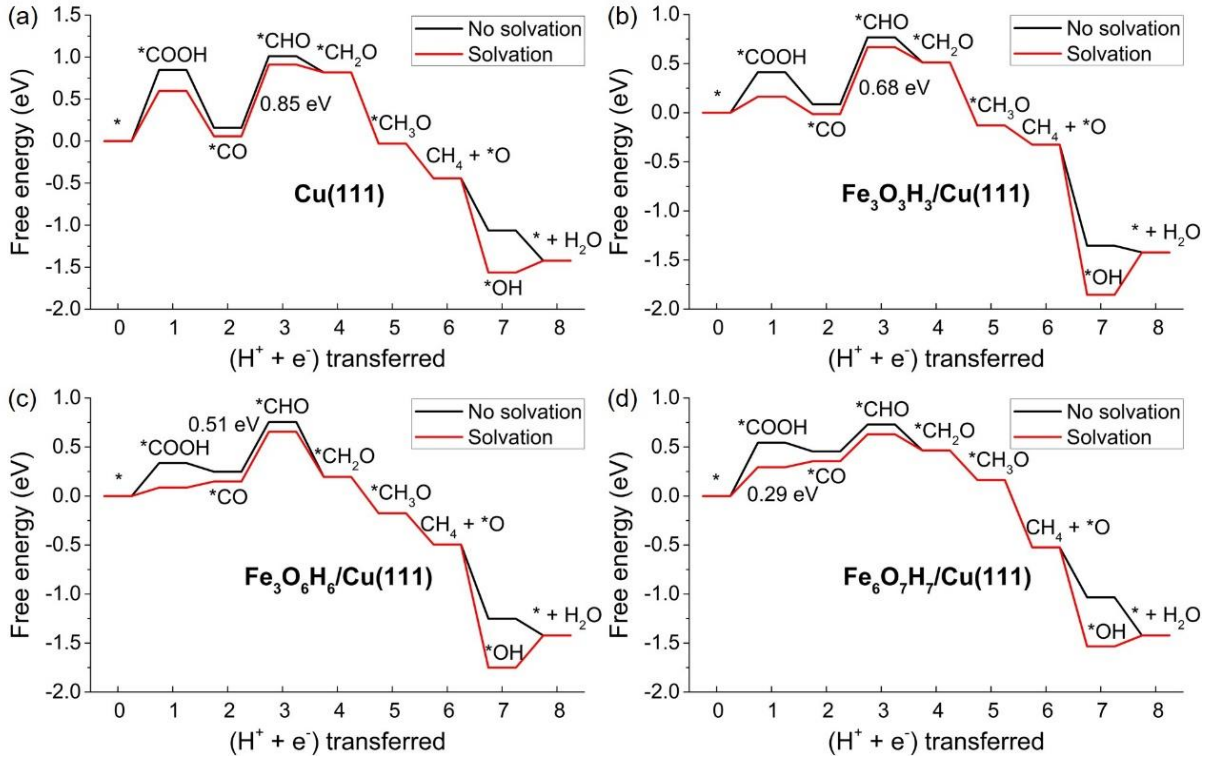

Fig. S16. Calculated free energy diagrams for CO_2RR on (a**)** Cu(111), (b) $Fe_3O_3H_3$/Cu(111), (c) $Fe_3O_6H_6$/Cu(111), and (d) $Fe_6O_7H_7$/Cu(111) with and without solvation corrections, respectively. The red and black solid lines represent the free energy pathways for CO_2RR with and without solvation corrections. The values in the subfigures indicate the energy barriers for the rate-limiting step of CO_2RR with solvation corrections for various possible FeO_x/Cu model catalysts. On the $Fe_3O_3H_3$/Cu(111), the rate-limiting step remains to be the protonation of *CO to *CHO with a free energy barrier of 0.68 eV. Surprisingly, the *CHO intermediate is significantly enhanced on $Fe_6O_7H_7$/Cu(111), changing the rate-limiting step to the first step of CO_2 activation to form *COOH intermediate with a ultralow limiting potential of 0.29 V as compared to 0.85 V on Cu(111).

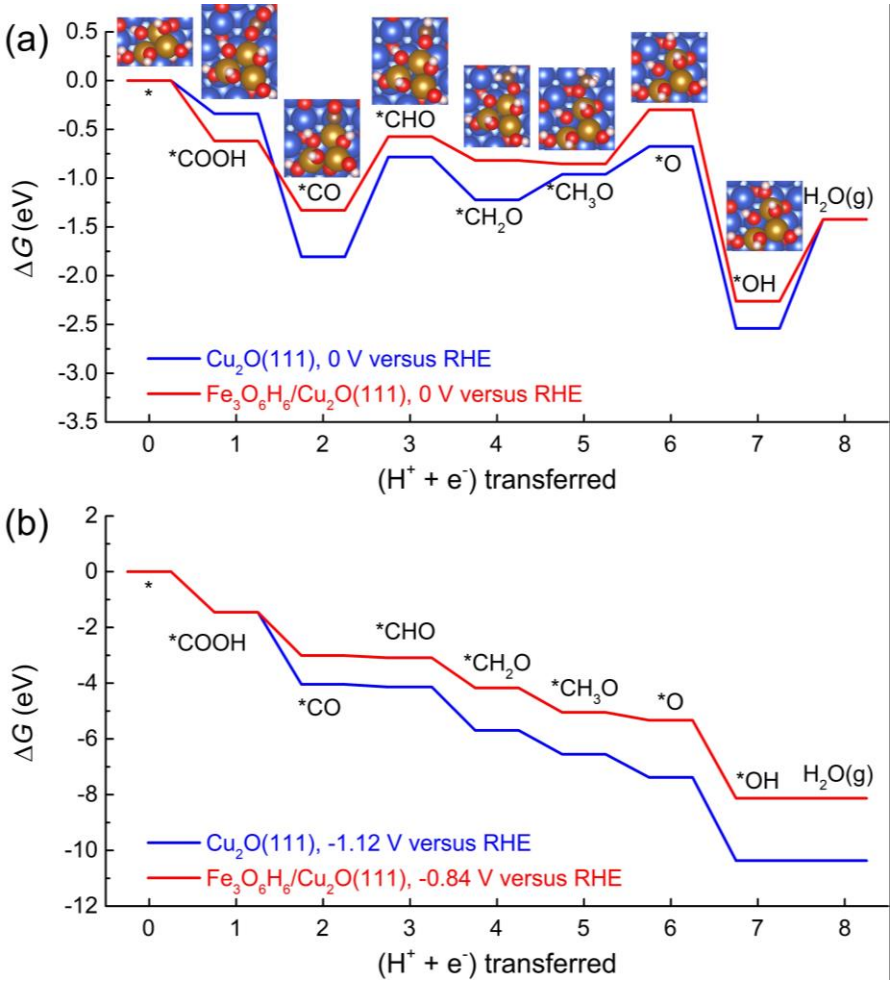

Fig. S17. Calculated free energy diagrams for CO_2RR on $Cu_2O(111)$ and $Fe_3O_6H_6/Cu_2O(111)$ under zero (a) and applied electrode potentials (b), respectively.

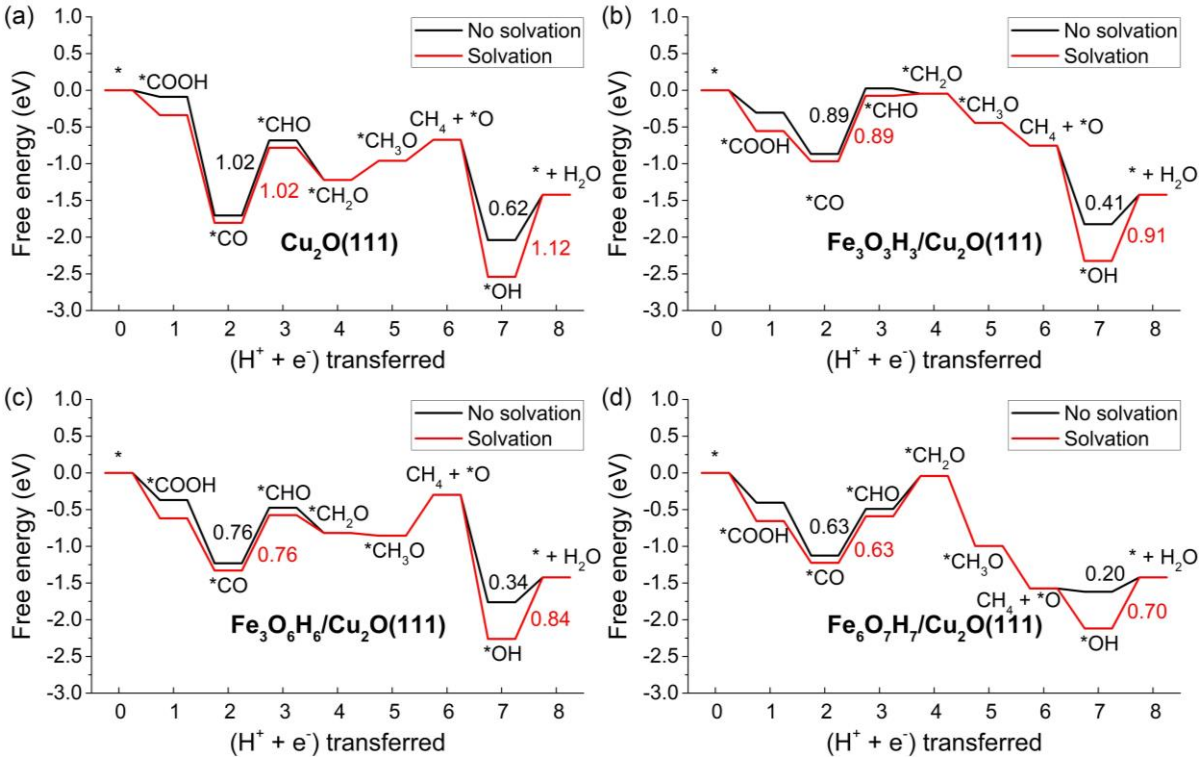

Fig. S18. Calculated free energy diagrams for CO_2RR on (a**)** $Cu_2O(111)$, (b) $Fe_3O_3H_3/Cu_2O(111)$, (c) $Fe_3O_6H_6/Cu_2O(111)$, and (d) $Fe_6O_7H_7/Cu_2O(111)$, respectively. The red and black solid lines represent the free energy pathways for CO_2RR with and without solvation corrections. The values in the subfigures indicate the energy barriers for the potential-limiting step of CO_2RR with and without solvation corrections for different Fe:O atomic ratios.

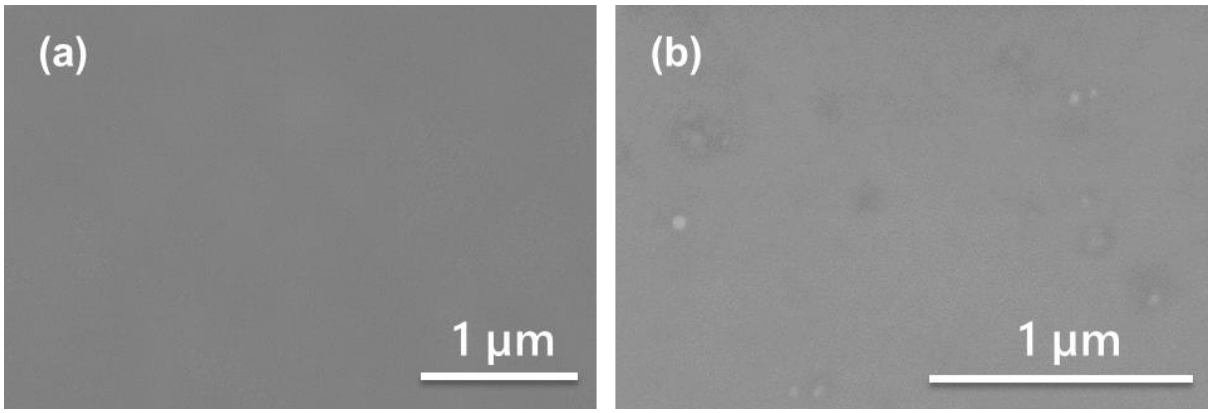

Fig. S19. SEM images of Si (a) and CuFe/Si (b).

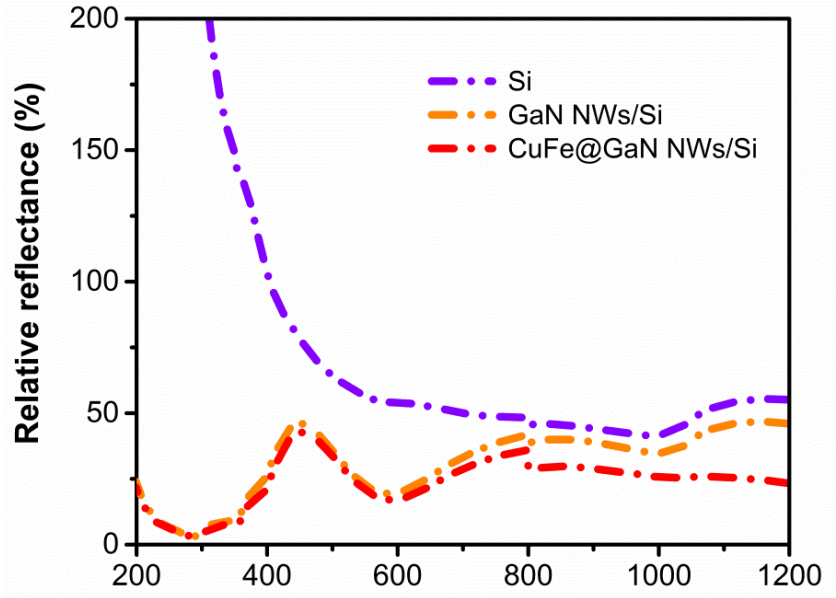

Fig. S20. Optical properties measurement of n^+-p Si junction, GaN NWs/Si, and CuFe@GaN NWs/Si based on UV-Vis relative differential reflectance spectroscopy.

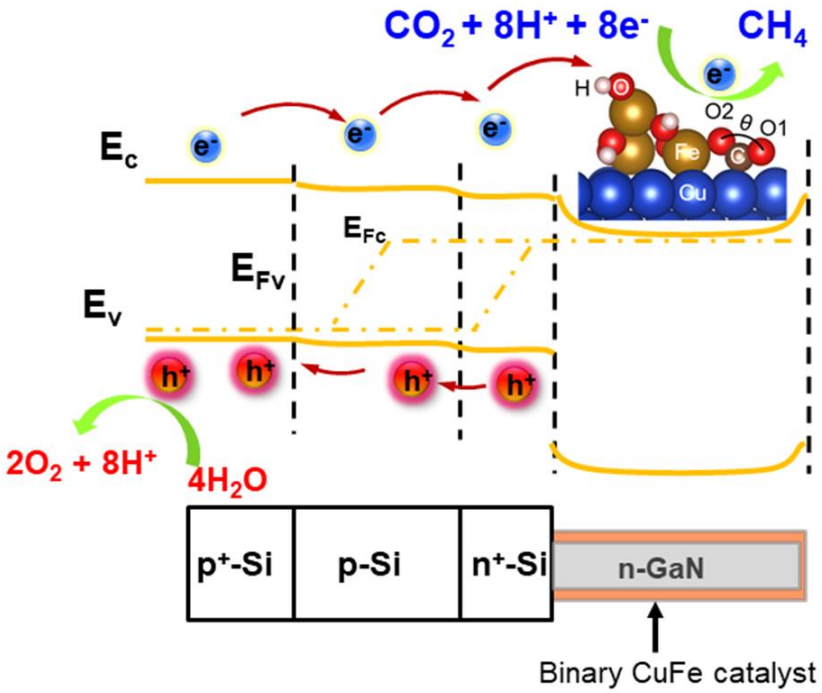

Fig. S21. Energy bandgap diagram of CuFe@GaN NWs/Si for PEC CO_2RR toward CH_4.

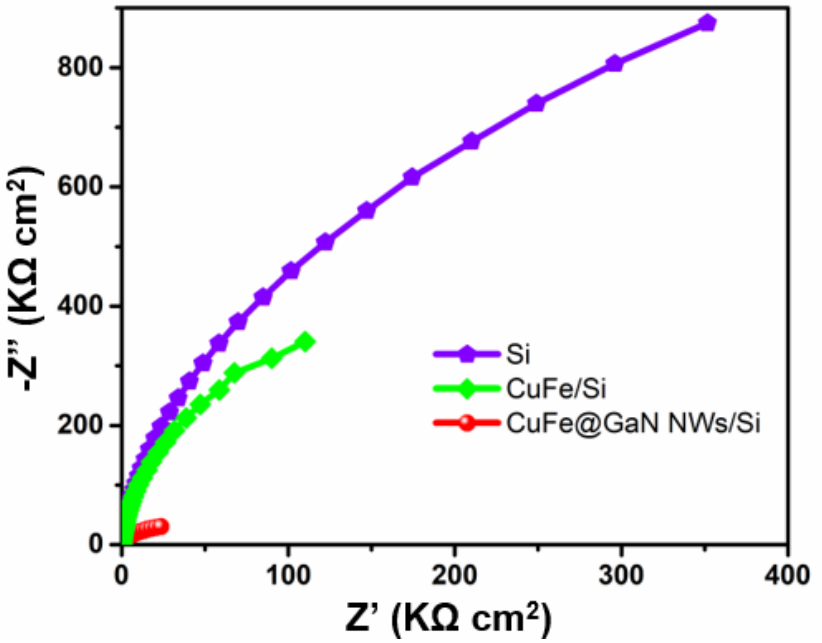

Fig. S22. Electrochemical impedance spectroscopy of n^+-p Si junction, CuFe/Si, and CuFe@GaN NWs/Si in CO_2-purged 0.5 M $KHCO_3$ aqueous solution under simulated solar light.

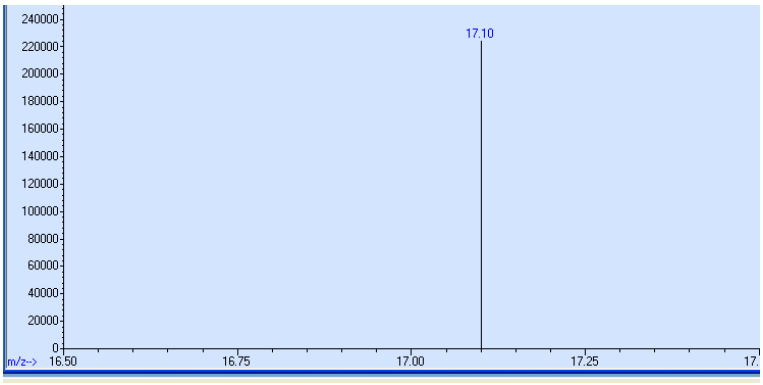

Fig. S23. Isotopic $^{13}CO_2$ labeled experiments. GC-MS spectra of the product obtained from ^{13}C-labeled bicarbonate aqueous solution (0.5mol/L) under $^{13}CO_2$ atmosphere.

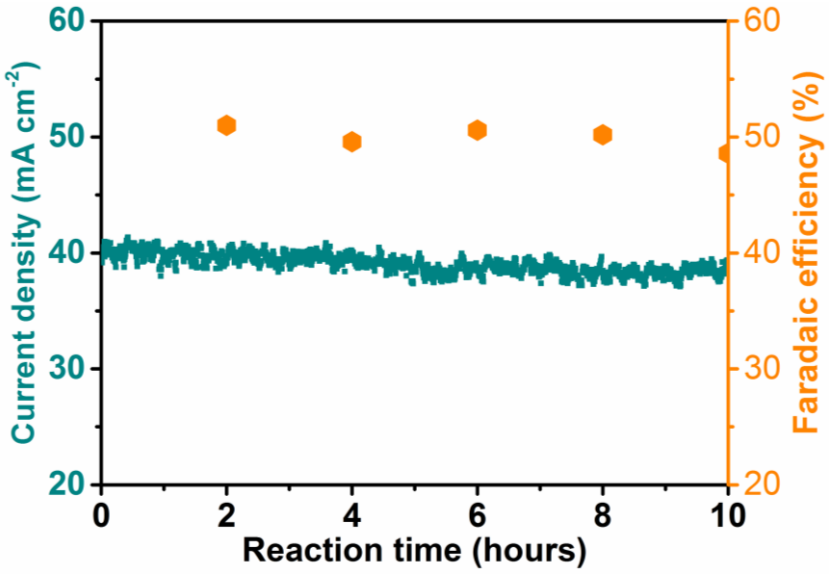

Fig. S24. Stability measurement of CuFe@GaN NWs/Si at -1.2 V under 1-sun illumination in CO_2-purged 0.5 M $KHCO_3$ aqueous solution. The right y axis is the Faradaic efficiency of methane.

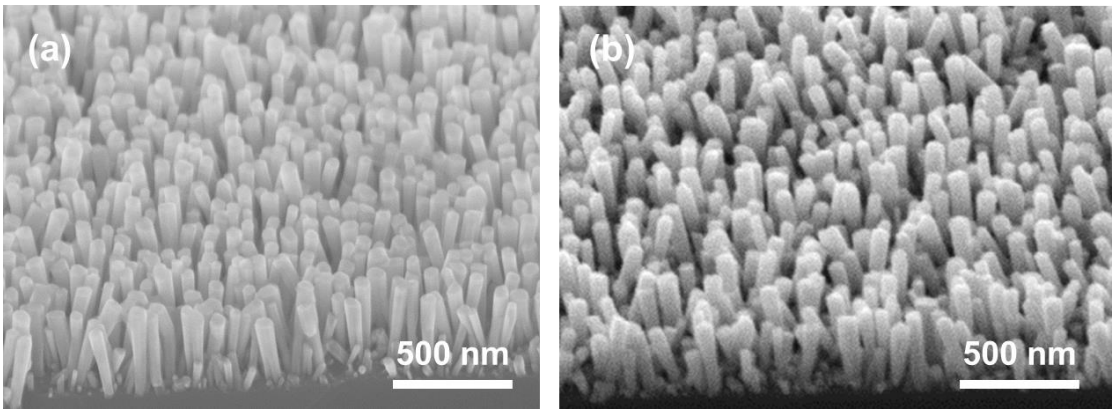

Fig. S25. SEM images of CuFe@GaN NWs/Si before (a) and after (b) 10 hours reactions at -1.2 V in CO_2-purged 0.5 M $KHCO_3$ aqueous solution under standard one-sun irradiation.